Transp Porous Med (2018) 123:257–270
https://doi.org/10.1007/s11242-018-1038-x

Permeability of Particle Soils Under Soil Pressure

Jichao Sun[1,2,3]

Received: 17 September 2017 / Accepted: 9 March 2018 / Published online: 16 March 2018

Abstract Soil is composed of particles that are condensed and bonded under an overburden pressure during burial. Obtaining the permeability coefficient of soil particles is an important issue in geological, geotechnical and hydraulic engineering. The permeability coefficient has been traditionally obtained by fitting data based on the particle size gradient and soil porosity. However, it is difficult to measure soil porosity, sample at certain depths and maintain the original pressure while sampling in the field and performing tests in the laboratory. The complicated nature of the experimental method results in considerable uncertainty regarding the accuracy of the permeability coefficient. In this paper, soil particles bonded by the force of gravity are modeled, with different pressures at different depths. Permeable soils form at certain depths, and the macroscopic permeability coefficient of the soil is obtained via seepage calculations. A relationship between the upper pressure and the permeability coefficient is established to remove the dependence on the porosity, which is an intermediate coupling parameter between soil particles and seepage. The results show that the modeled permeability coefficient is consistent with the results of previous models, and the permeability coefficient decreases with increasing depth. Thus, the proposed model of soil particle penetration can be directly used to calculate the permeability coefficient.

Keywords Permeability · Upper pressure · Particle soils

Many studies (Armstrong et al. 1991; Mathur and Levesque 1985; Naff and Vecchia 1987; Rose et al. 1965; Youngs 1965, 1971) have observed the phenomenon of the permeability

✉ Jichao Sun
Jichao@email.com; sjc00@126.com

1 School of Water Resource and Environment, China University of Geosciences, Beijing 100083, China

2 MOE Key Laboratory of Groundwater Circulation and Environmental Evolution, China University of Geosciences, Beijing 100083, China

3 Beijing Key Laboratory of Water Resources and Environmental Engineering, China University of Geosciences, Beijing 100083, China

coefficient decreasing with increasing burial depth. For example, the effect of the overburden weight on the water suction and hydraulic conductivity of soils was noted by Rose et al. (1965). Saar and Manga (2004) obtained the depth dependence of permeability in the Oregon Cascades based on the effects of thermal, seismic, hydrogeologic and magmatic modeling constraints. Sakata and Ikeda (2013) found that the decrease in permeability with depth was obvious in a middle alluvial fan above a depth of 30 m.

The permeability coefficient has a considerable influence on many physical parameters, such as water stratification (Davis and Turk 1964), Soil moisture between the land surface and the atmosphere (Brocca et al. 2009, 2013), mine water inflow (Zhang and Franklin 1993), dam seepage (Youngs 1965) and the groundwater level (Armstrong et al. 1991; Youngs 1971). The permeability coefficient is affected by many factors, such as different topographic trends (Ma et al. 2016). Additionally, heterogeneities in the permeability coefficient are associated with large and deep structural features (e.g., multiwatershed-scale and continental-scale features) and other influences (Welch and Allen 2014), such as faults (Chaussard et al. 2014; Reitsma and Kueper 1994) and faulting (Figueiredo et al. 2015; Rabbani and Jamshidi 2014; Rutqvist 2015), shallow fractured rock aquifers (Earnest and Boutt 2014; Figueiredo et al. 2015; Rabbani and Jamshidi 2014), lithology (Jayawardane and Blackwell 1991; Sakata and Ikeda 2013), different depositional environments (Rosas et al. 2014), the particle size distribution and bulk-density (Jabro 1992), different salt solutions (Jayawardane 1992), the soil distribution (Zhao et al. 2010), the terrain slope (Meyerhoff and Maxwell 2011; Min et al. 2013), the inhomogeneity of sedimentary structures (Bakshevskaya and Pozdnyakov 2013), and seasonal patterns (Rienzner and Gandolfi 2014) and directions (vertical and horizontal) (Dong et al. 2012; Min et al. 2013). As depth increases, the pressure from the above stratum gradually increases. These changes lead to porosity changes. Therefore, the permeability coefficient decreases with increasing depth, while the pressure increases with depth.

Under external pressure, the porosity and permeability of soils decrease. As the burial depth increases, the pressure gradually increases, whereas the permeability coefficient decreases. In the process of soil formation, the upper soil layer is gradually deposited and thickens; thus, the pressure is not instantly applied but gradual. Based on the formation process of seepage soils, above studies have investigated the relationships between upper-layer pressure and the permeability coefficient from qualitative and experimental perspectives. Therefore, the objective of this paper is to quantitatively evaluate the physical processes and physical meanings involved in these soil interactions. Namely, the relationship between the pressure of soil particles and the soil permeability coefficient is the focus of this paper.

1 Soil Particle Penetration Model

Many particles are connected together and the pores between particles are permeable, which is the fact. Soils contain many soil sections (soil blocks) that include small soil particles (as shown in Fig. 1). According to Fig. 1, a larger particle can consist of many smaller particles. Further, the smaller particle can consist of smaller, smaller particles, and so on (as some serious illustrations show in Fig. 1). According this process, the smallest particle is not permeable.

At some point, the smallest particles can no longer be divided into a smaller size group. These smallest particles are called meta-particles (original particles). This paper assumes that the meta-particles are impermeable, but the pores between these meta-particles are permeable, and the permeability of the soil is influenced by these pores. But according this process, it is very difficult to find the smallest particle. According the common rule, when the difference

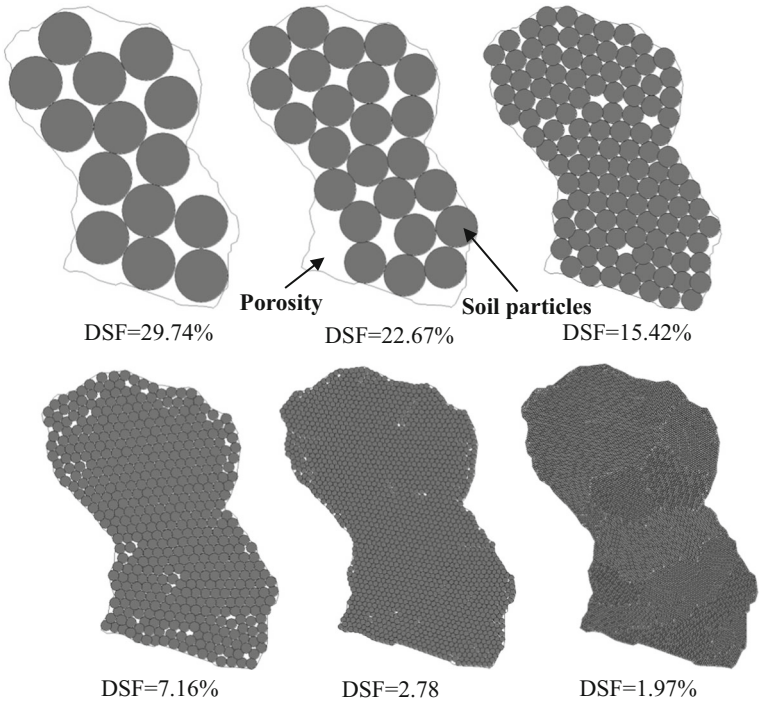

Fig. 1 Soils composed of particles of different sizes. DSF = (Fact area − Simulation area) × 100%/Fact area

between the simulation area and the area is < 5%, the simulation method is acceptable. So the difference is < 5%, the hypothesis is acceptable.

According to the assumption that the pores between the particles are permeable and the particles are impermeable. The water flow is in pores between the particles. The flow equations are Navier–Stokes equations. Navier–Stokes equations for incompressible flows are

$$\rho_{\mathrm{w}} \frac{\partial U}{\partial t} + \rho_{\mathrm{w}} U \cdot \nabla U = -\nabla P_{\mathrm{w}} + \nabla \cdot \left(\mu \left(\nabla U + (\nabla U)^T \right) \right)$$
$$\rho \nabla \cdot U = 0$$

where ρ_{w} is the water density (SI unit: kg/m^3); U is the velocity vector (SI unit: m/s); P_{w} is the water pressure (SI unit: Pa); μ is the dynamic viscosity (SI unit: Pa s); t is the time (SI unit: s).

Soils are composed of a large number of soil particles. Many soil particles have only one contact point with each other (Barreto and O'Sullivan 2012). This can be called contact bonding. In addition, some of the earth particles overlap, that is, there are multiple contact points which is called parallel bonding. The difference between the parallel bonding and the contact bonding is the distance between the two most recent contact points (as shown in Fig. 2a). When the distance is 0, it is the contact bonding, while when the distance is < 0, it is parallel bonding. The contact bonding is a special case of the parallel bonding. The parallel bond is similar to the physical behavior of the cement—like substance between particles, which is located between two bonded particles and connects the two bonding. The parallel bonds create an elastic interaction between these particles. The parallel bond can transfer the

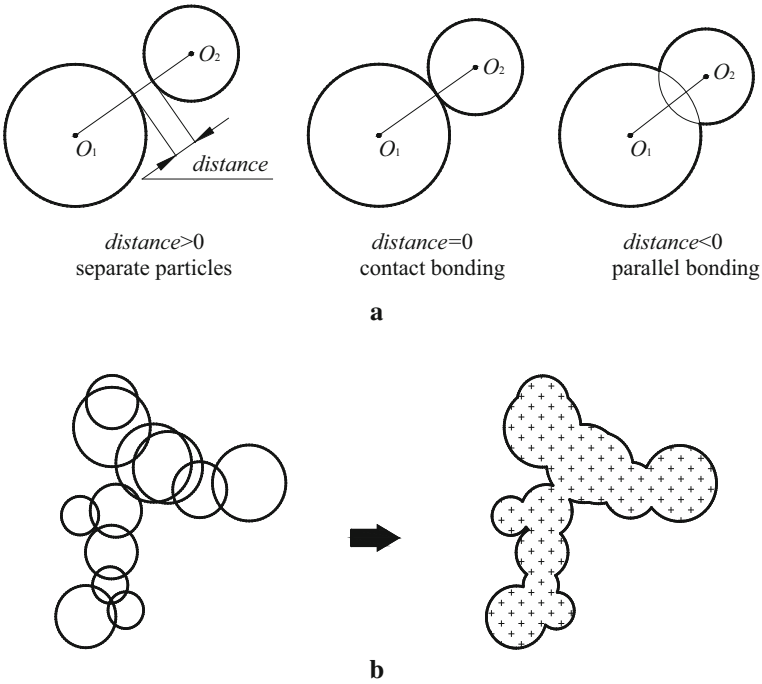

Fig. 2 Parallel bond model of soil particles. **a** Particles bonding. **b** soils established by particles by parallel bonding

force and moment between the particles, but contact bonds can only transfer the force on the contact point. This paper takes a parallel bonding shown in Fig. 2.

These small particles continue to accumulate and concentrate due to the upper pressure. Some small particles can become connected. Thus, with increasing depth and pressure, the pore space and permeability of the soil gradually decrease.

In this paper, a particle penetration model is established to study the variability in the permeability coefficient with depth. The model of soil particle penetration under the upper pressure is established.

The process of the establishment has two steps: (step 1) establish particle soils, for example, the sample is $x \in [0, 10\ \text{mm}]$, $y \in [0, 10\ \text{mm}]$; apply upper solid pressure, the pressure is equal to the upper soils weight. The particle is pressed. The height of sample decreases after pressing. Then pick up the new position of every particle. (step 2) establish the new particle soil from step 1 new position of particles, then simulate water flow. Then obtain the velocity and export total discharge. The average velocity can be obtained according the export total discharge. According to the Darcy law format and the average velocity, obtain the permeability coefficient. In these two steps, the upper pressure and depth have the connection with the permeability coefficient.

The soils in some certain depth are pressed by the upper soils pressure. The upper soils pressure is $P = \boldsymbol{\rho g h}$, where $\boldsymbol{\rho}$ is the density of the particles, $\boldsymbol{g}$ is gravitational acceleration, $\boldsymbol{h}$ is the particle soil depth. The deeper the depth of the soil is, the greater the upper pressure P (as shown in Fig. 3). The particles are gradually condensed and concentrated, and the pores between the particles are gradually reduced. The soils in h miters are pressed by upper h meters soils weight. In order to simulate the upper pressure, the soil sample, width = 10 mm, height = 10 mm, is chosen to be pressed, as shown in Fig. 3. Figure 3 establishes the horizontal

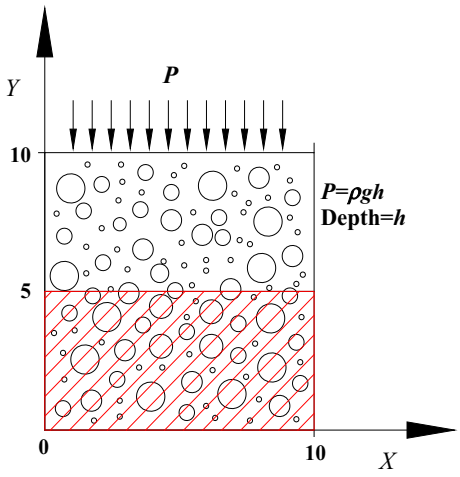

Fig. 3 Pressing of particulate soil. Step 1 in the model of soil particle penetration. Where P is the upper pressure of soils; $\boldsymbol{\rho}$ is the density of the particles; $\boldsymbol{g}$ is gravitational acceleration; $\boldsymbol{h}$ is the soils depth; The part shaded in red, $x \in [0, 10\text{ mm}]$ and $y \in [0, 5\text{ mm}]$, is chosen to carry out the permeability test after soils pressed

and vertical axes, which are X and Y coordinate axis in order to introduce more clearly. The part shaded in red, $x \in [0, 10\text{ mm}]$, $y \in [0, 5\text{ mm}]$, is chosen to carry out the permeability test after soils are pressed by h meters soils weight. The h meters soils weight is ρgh, that is P.

The elastic modulus and Poisson's ratio can then be obtained. The forces F_x and Fy are applied in both directions, and the stress is given by σ_x and σ_y. The strain formulas are presented in Eqs. (1) and (2):

$$\varepsilon_x = \frac{1}{E}\left(\sigma_x - \upsilon\sigma_y\right) \tag{1}$$

$$\varepsilon_y = \frac{1}{E}\left(\sigma_y - \upsilon\sigma_x\right) \tag{2}$$

These equations form the plane strain problem, namely, $\varepsilon_x = 0$; therefore, $\sigma_x = \upsilon\sigma_y$ and $\sigma_x + \Delta\sigma_x = \upsilon(\sigma_y + \Delta\sigma_y)$ satisfy Eq. (3):

$$\Delta\sigma_x = \upsilon\Delta\sigma_y \tag{3}$$

when a small force ΔFy is applied, the corresponding ΔFx and Δy can be determined. Then, $\varepsilon_y = \Delta y/y$ is obtained. Additionally, the Poisson's ratio υ and elastic modulus of E can be obtained according to Eqs. (1), (2) and (3), where $\sigma_x = Fx/y$, $\sigma_y = Fy/x$, $\Delta\sigma_x = \Delta(Fx/y)$, and $\Delta\sigma_y = \Delta(Fy/x)$.

Where F_x, Fy are the force applied on the sample in x- and y-direction; ΔFy, ΔFy are the force increment, when the soil are stable under the force F_x and Fy; σ_x and σ_y are the stress on the sample in x- and y-direction; ε_y and ε_y are the strain on the sample in x- and y-direction; υ is the Poisson's ratio; E is the elastic modulus; x, y are the sample width and height after pressing under force.

After determining the radii of particles at a certain depth h and pressure P (such as the red region in Fig. 3), the soil particle class can be established (Fig. 4a, b).

The particles are impermeable, and the pores between the particles are permeable. The model is two dimensional simulation, and the pore between particles are not connected. But the seepage occurs in three dimension simulation in fact. So the particle radius needs to be reduced by a coefficient reduction. In this way, it is possible to penetrate in two dimensional state. Of course, the coefficient needs a more rigorous choice in practices. In this paper, 0.6 is chosen. So the water flow in the pore between the particles. The pore, not particles, is

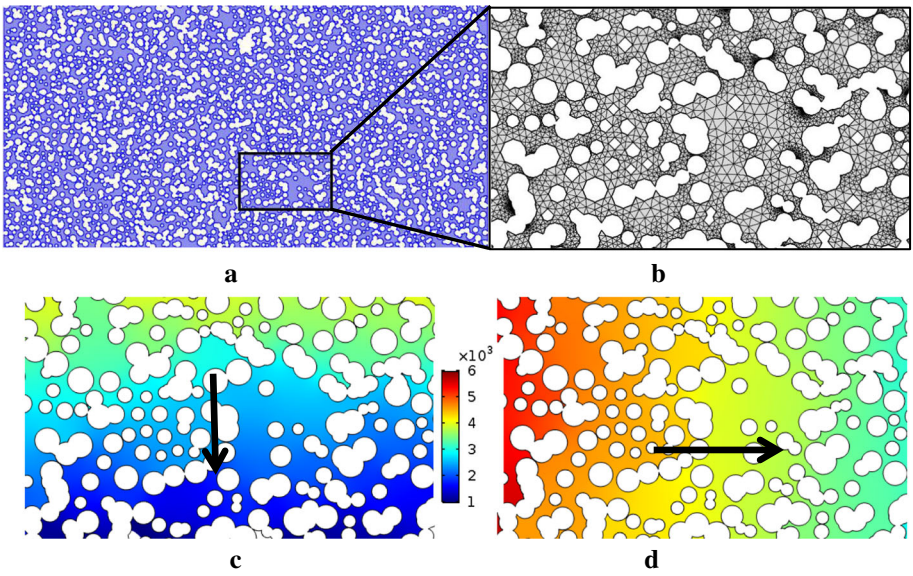

Fig. 4 Calculation of particulate soil penetration. **a** Calculated sample, which is the red part in Fig. 3; **b** finite element; **c** pressure of the flow from the top to the bottom; **d** pressure of the flow from the left to the right. The black narrow arrows are the flow directions. **b–d** The black frame region in **a**. The legend unit is Pa. The part shaded in red in Fig. 3 is the **a**. Step 2 in the model of soil particle penetration

meshed by the finite element meshing to simulate the eater flow. The finite element meshing is performed using the established pores (shown in Fig. 4b). The triangular elements are chosen, as show in Fig. 4b. Five kinds of mesh accuracy are chosen, and the ratios between the element size and calculated region width are (A) 4.08×10^{-3}–2.04×10^{-1}, (B) 6.12×10^{-4}–1.37×10^{-1}, (C) 6.12×10^{-4}–1.08×10^{-1}, (D) 2.56×10^{-4}–7.54×10^{-2} and (E) 1.53×10^{-4}–4.08×10^{-2}. The max error for the last permeability coefficient less than 1%. So the result of choosing mesh accuracy (B) is acceptable. The mesh accuracy (B) model scale of the element size is from 3.06×10^{-6} m to 6.83×10^{-4} m. The total quality of elements is 390,251.

The overall permeability of soils is associated with two directions. By applying a larger water pressure ΔP_{tb} at the upper boundary of the soil compared to that at the bottom boundary, infiltration occurs from top to bottom (shown in Fig. 4c). Additionally, by applying a larger water pressure ΔP_{lr} to the left boundary of the soil than to the right boundary, infiltration occurs from left to right (shown in Fig. 4d).

From Fig. 4, there are more sophisticated grid near the particle turning point in Fig. 4b. Figure 4c, d shows that the pressure is distributed along the flow direction from the height pressure to the low pressure. Particles block the water flow. After water flow runs through the little pores between particles, the water pressure changes little in a bigger pores. This shows that the particles are the main obstacles for the water flow.

The permeability coefficient of the entire soil obtained according to this research model is called the generalized permeability coefficient K. The generalized permeability coefficient is divided into two directions, and the associated formulas are given in Eqs. (4) and (5).

$$K_x = \frac{\rho_w g}{\Delta P_{lr}} \frac{L_{lr}}{L_{tb}} \int v_{rx} dy \tag{4}$$

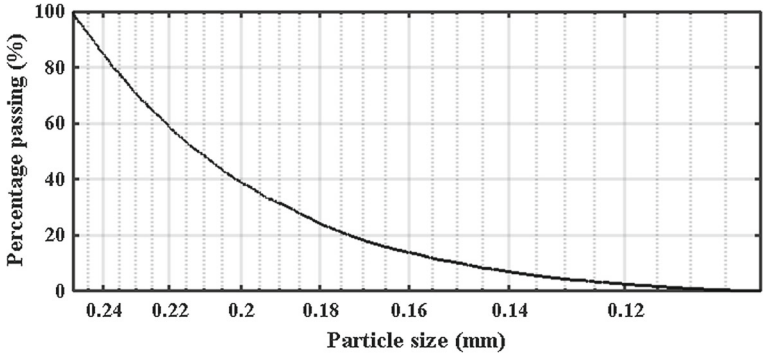

Fig. 5 Particle gradation curve

$$K_y = \frac{\rho_w g}{\Delta P_{tb}} \frac{L_{tb}}{L_{lr}} \int v_{by} dx \tag{5}$$

where K_x and K_y are the generalized permeability coefficients in the x- and y-directions, respectively; ρ_w is the water density; g is gravitational acceleration; L_{lr} is the length and distance from the left boundary to the right boundary of the particle soil sample in Figs. 3 and 4a; L_{tb} is the length and distance from the top boundary to the bottom boundary of the particle soil sample in Figs. 3 and 4a; ΔP_{lr} is the water pressure difference between the left and right boundaries of the soil when the infiltration direction is from the left to the right; ΔP_{tb} is the water pressure difference between the top and bottom boundaries of the soil when the infiltration direction is from the top to the bottom; v_{rx} is the x-direction velocity on the right exit boundary, shown by the black arrow direction in Fig. 4d; $\int v_{rx} \mathrm{d}y$ is the overall flow velocity in the x-direction, $\int v_{rx} \mathrm{d}y / L_{tb}$ is the average velocity in the x-direction on the right boundary; and v_{by} is the y-direction velocity on the bottom exit boundary, shown by the black arrow direction in Fig. 4c; $\int v_{by} \mathrm{d}x$ is the overall flow velocity in the y-direction; $\int v_{by} \mathrm{d}x / L_{lr}$ is the average velocity in the y-direction on the bottom boundary.

2 Example

Here, an example is presented to illustrate the calculation and analysis process. The particle quantity is 4000, the radius is $R \in [0.05007343, 0.12498922]$ and the unit is mm. The random particle soils are established in the range of $x \in [0, 10]$, $y \in [0, 10]$. The density of the particles is ρ = 2000 kg/m^3, and the normal stiffness of particles is 10^6 Pa/m. These parameters are used to establish the parallel bond model of the soil. After upper compression, the soils in $x \in [0, 10]$, $y \in [0, 5]$ are chosen to calculate the permeability coefficient. Four thousand particles are used to perform the particle analysis, and d_{10} is 0.1493 mm. The particle gradation curve is shown in Fig. 5.

pb_rad is the radius multiplier, such that parallel bond radius equals **pb_rad** multiplied by the minimum radius of the two contacting particles. **pb_kn** is the normal stiffness = 1e8 Pa/m; **pb_ks** is the shear stiffness = 1e8 Pa/m; **pb_nstrength** is the normal strength = 1e10 Pa; **pb_sstrength** is the shear strength = 1e10 Pa; and ***g*** is gravitational acceleration = 9.81 m/s^2.

The calculated results are shown in Fig. 6. Figure 6 illustrates the water pressure at the burial depth of 80 m, with P_l = 10,000 Pa at the left boundary and P_r = 0 at the right boundary. In Fig. 6, the pressure gradually decreases from left to right, and water moves in the porous medium.

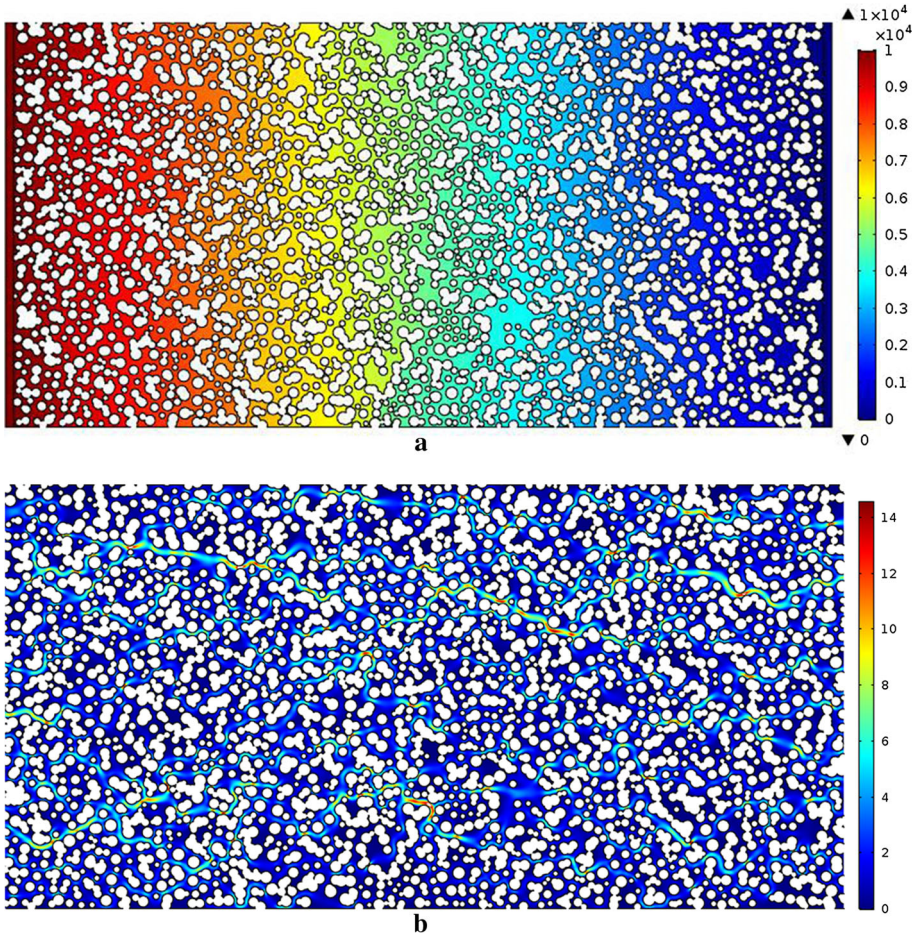

Fig. 6 Water pressure and velocity distribution in the soil at a depth of 80 m. **a** The water pressure distribution in the soil (Pa); **b** the velocity distribution in the soil (m/s). The top boundary and bottom boundary are the wall boundary. The left boundary is the inlet, on which boundary the pressure is 10^4 Pa. The right boundary is the outlet, on which boundary the pressure is 0 Pa

After pressing separately by the upper 0, 20, 80 and 100 m depth solid pressure, the pore between particles decreases.

The gray images of the porosity distribution at different depths are shown in Fig. 7. The sample is divided into 200 pieces of 0.5 mm × 0.5 mm small rectangular grid. In every rectangle, the pore area is calculated. The porosity is equal to the ratio between the pore area and grid area 0.5 mm × 0.5 mm.

The height of the sample is monitored during compressing. According to Eqs. (1), (2) and (3), Poisson's ratio and the elastic modulus can be calculated. The soils in $x \in [0, 10\text{ mm}]$, $y \in [0, 5\text{ mm}]$ are chosen from the compressed soils to calculate the actual porosity. Additionally, the seepage coefficient of the soil in horizontal direction is calculated, and the results are shown in Table 1.

H_d is the burial depth (m); P is the upper pressure of soils (Pa); $\boldsymbol{\rho}$ is the density of the particles, $\rho = 2000\text{ kg/m}^3$; $\boldsymbol{g}$ is gravitational acceleration = 9.81 m/s^2; $\boldsymbol{h}$ is the particles depth; error(%) is abs$(\rho gh - P) \times 100\%/(\rho gh)$, abs is the absolute value; E_f is the ratio between

Table 1 Mechanical parameters, permeability coefficients and porosities at different depths

H_d	P	ρgh	Error (%)	E_f	H_2	S	υ	E	n	$\int v_{rx}dy$	K
0	0	–	–	–	10	18.672	–	–	0.63	0.522	1.025
10	196,784	196,200	0.30	2.117	8.374	20.083	0.031	1.44E+06	0.60	0.485	0.952
20	391,216	392,400	0.30	2.166	7.917	21.054	0.071	1.69E+06	0.58	0.460	0.902
50	983,136	981,000	0.22	2.23	7.023	23.578	0.100	1.70E+06	0.53	0.378	0.742
80	1,572,312	1,569,600	0.17	2.283	6.467	25.288	0.137	1.77E+06	0.49	0.326	0.640
90	1,770,076	1,765,800	0.24	2.347	6.322	25.814	0.21	1.98E+06	0.48	0.307	0.603
100	1,960,784	1,962,000	0.06	2.373	6.15	26.478	0.292	2.61E+06	0.47	0.289	0.567

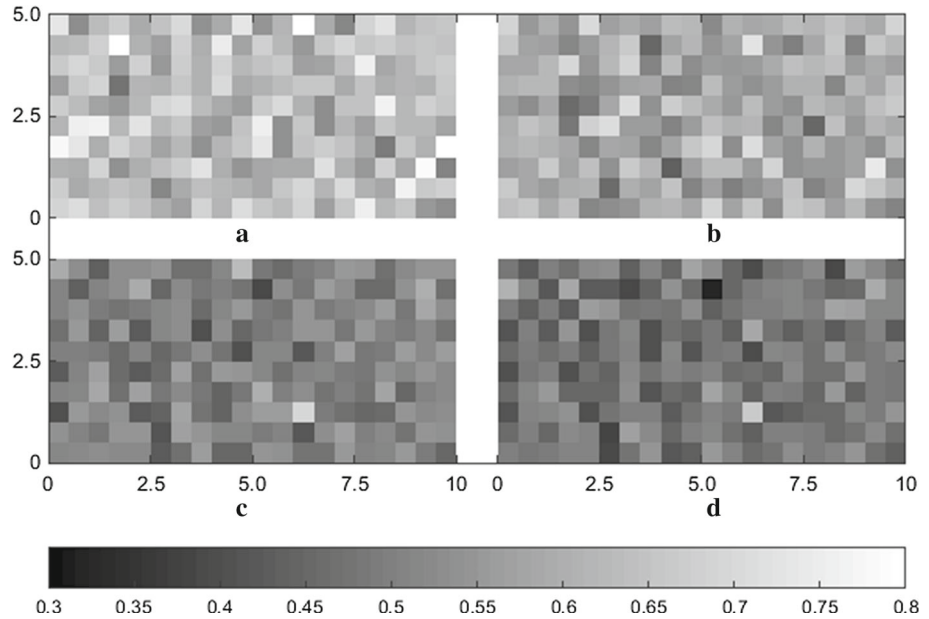

Fig. 7 Gray images of the porosity distribution at different depths. The units of the X and Y axes are mm. **a–d** The gray images at depths of 0, 20, 80 and 100 m, respectively

the vertical force and the horizontal force; H_2 is the sample height (mm) after compression; S is the total area of particles (mm^2); υ is Poisson's ratio and it is obtained from Eqs. (1), (2) and (3); E is the elastic modulus (pa) and it is obtained from Eqs. (1), (2) and (3); n is the porosity, $n = e/(1 + e)$, e is the porosity ratio; $\int v_{rx} dy$ is the overall flow velocity in the x-direction (10^{-2} m^2/s), and it can be obtained from Fig. 6b; and K is the permeability coefficient in the horizontal direction (cm/s, or 10^{-2} m/s), and it is obtained from Eq. (4).

There are some errors between the P/pa and ρgh. In the process of pressing the particles under the upper pressure, particles force in fact is not absolutely equal to the requirement force, because the soils composite of particles are heterogeneous soils. The force between particles has some small fluctuation. From the pressure error in Table 1, the last pressure (P/pa) is acceptable.

3 Discussion and Analysis

In Fig. 7: (a) the porosities of a–d are different. Specifically, different locations have different porosities, and these porosities exhibit considerable randomness because the particles of composite soils exhibit overlap, occlusion and contact. (b) The gray images of a–d darken and the porosity gradually decreases as pressure and depth increase. (c) At the same position but different depths, the gray color nearly changes to black. Additionally, porosity is negatively correlated with depth.

The formula of the Terzaghi permeability coefficient is as follows:

$$K = 2d_{10}^2 e^2 = 2d_{10}^2 \left(\frac{n}{1-n}\right)^2 \tag{6}$$

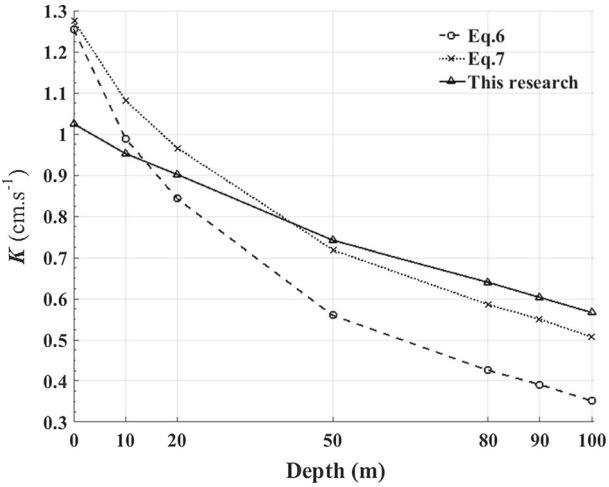

Fig. 8 The relationship between the permeability coefficient and depth based on different formulas

where d_{10} is the particle size corresponding to 10% of the particle size distribution curve (mm) and e is the porosity ratio. The unit of K is cm/s.

The formula of the Darcy permeability coefficient is as follows:

$$K = \frac{\beta \gamma_{wz}}{\lambda \eta} \frac{e^2}{1+e} d^2 \tag{7}$$

where d is the particle diameter (cm); β is the spherical particle coefficient, which is $\pi/6$ when the particle is a sphere; λ is the influence coefficient of adjacent particles, which is 3π when the particle is infinitely adjacent to water; γ_{wz} is the density of free water (kN/m^3); η is the viscosity coefficient of water (Pa s); and e is the porosity ratio. The unit of K is cm/s.

Equation (7) can be used in soils composite of sand soils that is called coarse-grained soils. The coarse-grained soils which of the particles larger than 0.1 mm is accounted for the majority that is > 50%. From Fig. 5, the percent of the particles larger than 0.1 mm is 98% > 50%. It is concluded through a large number of experiments. This equation is widely used in hydraulic engineering, geotechnical engineering and groundwater engineering. Macroscopically, this kind of sols is homogeneous soil. Microscopically, this kind of sols is heterogeneous soil. Equation (7) can be used in this kind of soils in this research.

In the example, $d_{10} = 0.1493$ mm, $d = 0.01493$ cm, $\eta = 0.001$ Pa s, and $\gamma_{wz} = 9.81$ kN/m^3. From Eqs. (6) and (7) and the porosity ratio in Table 1, the permeability coefficient in the horizontal direction can be calculated, as shown in Fig. 8.

Equations (6) and (7) are equations of the porosity and permeability coefficient based on field sampling and laboratory experiments. The applicable materials include non-cohesive soil particles and sand particles. When the porosity is large, large pores exist between particles. The flow in these pores may reach a turbulent state, causing the flow velocity to greatly increase. However, the flow velocity decreases rapidly when the porosity decreases. Therefore, the ratio of the porosity to the permeability coefficients varies considerably in space.

And from the result, the *Re* of the element is calculated. The max *Re* is about 348 about in (5.08, 1.20 mm). The max *Re* = 348 is less than 2300, so the flow can be treated as Laminar Flow (Brackbill et al. 2006). Thus, no turbulence is present, and the flow velocity is relatively

stable. In this paper, in spite of the flow is Laminar Flow, the porosity is treated as the Darcy flow [as shown in Eqs. (4) and (5)] to obtain the permeability coefficient.

Table 1 shows that the porosity of the soil decreases gradually with increasing depth. Additionally, the results illustrated in Fig. 8 show that the permeability coefficient decreases with increasing depth, and the three curves are similar. This result suggests that the computational process and the model of soil particle penetration are reliable.

In Fig. 8, the curves of Eqs. (6) and (7) are steeper than that of the model. In addition, the curve of this research intersects the other two curves of Eqs. (6) and (7), and as depth increases, the curves of Eqs. (6) and (7) gradually separate.

The following is the explanation of the associated physical mechanism. By substituting $e = n/(1 - n)$ into Eq. (7), the following expression can be obtained.

$$K = \frac{\beta \gamma_{wz}}{\lambda \eta} \frac{n^2}{1 - n} d^2 \tag{8}$$

From Eqs. (6) and (8), as the depth increases, n decreases and increases gradually; thus, the results of Eqs. (6) and (7) gradually separate, where K_6 and K_7 are the results of Eqs. (6) and (7), respectively.

In the process of the granular soil compression, the particles are connected by parallel bonding. The normal strength and shear strength in this paper are 10^{10} Pa. This strength is relatively large. Under the applied upper pressure, the particle connections are not easy to break; therefore, the porosity remains high, and the slope of the model curve is moderate.

The porosity and permeability coefficient calculated using Eqs. (6) and (7) are based on laboratory results and field sampling. These equations apply to non-cohesive soil particles and sands. When the porosity is large, large pores exist between soil particles. The flow volume along the central axis of a pore is higher than that in the rest of the pore, resulting in a larger seepage velocity. By contrast, when the porosity decreases, the seepage velocity decreases. This is not the case for the model proposed in this paper. Therefore, at shallow depths, the permeability coefficient of the model is smaller than those obtained based on Eqs. (6) and (7). However, at deeper locations in the soil, the permeability coefficient of the model is larger than those of Eqs. (6) and (7).

Figure 9 illustrates that the permeability coefficient decreases with increasing depth (Maftei and Barbulescu 2006; Saar and Manga 2004). Additionally, the elastic modulus and Poisson's ratio increase with increasing depth, and the elastic modulus increases at a faster rate than does Poisson's ratio.

The following is the explanation of the associated physical mechanism. As depth increases, the pores between the particles gradually decrease in size, and the contact area and number of particles increase. When the same external force is applied, the deformation is smaller; therefore, the elastic modulus is larger. For a constant compression of soil particles, the compactness increases. When subjected to the same vertical deformation, lateral deformation increases, which causes Poisson's ratio to increase.

4 Conclusions

In this study, the macroscopic permeability coefficient of soils is successfully determined using a model of soil particle penetration. This method overcomes the limitations of traditional methods and provides a useful approach to obtaining the permeability coefficient.

The pressure calculation of particle flow is combined with a finite element calculation of seepage in the medium. The results show that the soil porosity and the permeability

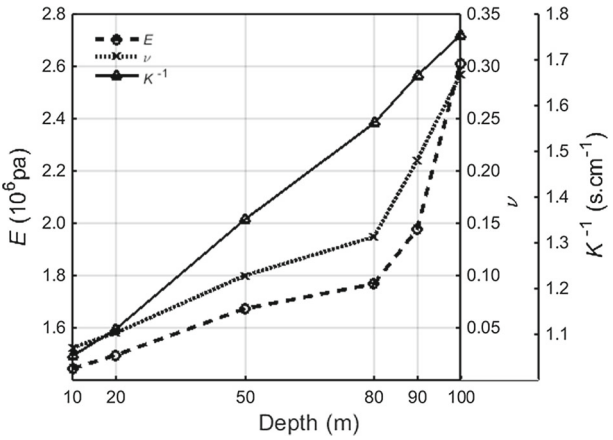

Fig. 9 The elastic modulus, Poisson's ratio and permeability coefficient at different depths

coefficient decrease when pressure is applied to the upper boundary of the soil. Additionally, the permeability coefficient decreases with increasing soil depth, which is consistent with the results from the literature (Maftei and Barbulescu 2006; Saar and Manga 2004). Moreover, the elastic modulus and Poisson's ratio gradually increase with depth, and the associated the mechanism is discussed.

In addition, a given geometric properties (such as the particle radius, the particle position, the porosity and the particle quantity) different realization of geometry could be obtained numerically. The permeability of each of those realizations is perhaps different. This research does not fully consider this. Future researchers can continue to study this phenomenon and its laws.

Funding Funding was provided by Fundamental Research Funds for the Central Universities (Grant No. 2652017164).

Compliance with Ethical Standards

Conflict of interest The author declares that he has no conflict of interest.

References

Armstrong, A.C., Youngs, E.G., Arrowsmith, R.: Modeling water-table movement in drained soils with depth-dependent hydraulic conductivity. Agric. Water Manag. **20**(2), 101–108 (1991)

Bakshevskaya, V.A., Pozdnyakov, S.P.: Methods of modeling hydraulic heterogeneity of sedimentary formations. Water Resour. **40**(7), 667–775 (2013)

Barreto, D., O'Sullivan, C.: The influence of inter-particle friction and the intermediate stress ratio on soil response under generalised stress conditions. Granul. Matter **14**(4), 505–521 (2012)

Brackbill, T.P., Kandlikar, S.G., ASME: Effect of Triangular Roughness Elements on Pressure Drop and Laminar–Turbulent Transition in Microchannels and Minichannels. Amer Soc Mechanical Engineers, New York (2006)

Brocca, L., Melone, F., Moramarco, T., Morbidelli, R.: Soil moisture temporal stability over experimental areas in Central Italy. Geoderma **148**(3–4), 364–374 (2009)

Brocca, L., Tarpanelli, A., Moramarco, T., Melone, F., Ratto, S.M., Cauduro, M., Ferraris, S., Berni, N., Ponziani, F., Wagner, W., Melzer, T.: Soil moisture estimation in alpine catchments through modeling and satellite observations. Vadose Zone J. **12**(3), 10 (2013)

Chaussard, E., Burgmann, R., Shirzaei, M., Fielding, E.J., Baker, B.: Predictability of hydraulic head changes and characterization of aquifer-system and fault properties from InSAR-derived ground deformation. J. Geophys. Res. Solid Earth **119**(8), 6572–6590 (2014)
Davis, S.N., Turk, L.J.: Optimum depth of wells in crystalline rocks. Groundwater **2**(2), 6–11 (1964)
Dong, W., Chen, X., Wang, Z., Ou, G., Liu, C.: Comparison of vertical hydraulic conductivity in a streambed-point bar system of a gaining stream. J. Hydrol. **450–451**(15), 9–16 (2012)
Earnest, E., Boutt, D.: Investigating the role of hydromechanical coupling on flow and transport in shallow fractured-rock aquifers. Hydrogeol. J. **22**(7), 1573–1591 (2014)
Figueiredo, B., Tsang, C.F., Rutqvist, J., Niemi, A.: A study of changes in deep fractured rock permeability due to coupled hydro-mechanical effects. Int. J. Rock Mech. Min. Sci. **79**, 70–85 (2015)
Jabro, J.D.: Estimation of saturated hydraulic conductivity of soils from particle-size distribution and bulk-density data. Trans. ASAE **35**(2), 557–560 (1992)
Jayawardane, N.S.: Prediction of unsaturated hydraulic conductivity changes of a loamy soil in different salt-solutions by using the equivalent salt-solutions concept. Aust. J. Soil Res. **30**(5), 565–571 (1992)
Jayawardane, N.S., Blackwell, P.S.: Relationship between equivalent salt solution series of different soils. J. Soil Sci. **42**(1), 95–102 (1991)
Ma, R., Shi, J., Zhang, Y., Sun, L.: Variation of hydraulic conductivity with depth in the North China plain. Arab. J. Geosci. **9**(10), 1–13 (2016)
Maftei, C., Barbulescu, A.: Modeling the relation between the hydraulic conductivity and the depth. Paper presented at the mathematical modelling of environmental and life sciences problems (2006)
Mathur, S.P., Levesque, M.: Negative effect of depth on saturated hydraulic conductivity of histosols. Soil Sci. **140**(6), 462–466 (1985)
Meyerhoff, S.B., Maxwell, R.M.: Quantifying the effects of subsurface heterogeneity on hillslope runoff using a stochastic approach. Hydrogeol. J. **19**(8), 1515–1530 (2011)
Min, L., Yu, J., Liu, C., Zhu, J., Wang, P.: The spatial variability of streambed vertical hydraulic conductivity in an intermittent river, northwestern China. Environ. Earth Sci. **69**(3), 873–883 (2013)
Naff, R.L., Vecchia, A.V.: Depth-averaging effects on hydraulic-head for media with stochastic hydraulic conductivity. Water Resour. Res. **23**(4), 561–570 (1987)
Rabbani, A., Jamshidi, S.: Specific surface and porosity relationship for sandstones for prediction of permeability. Int. J. Rock Mech. Min. Sci. **71**, 25–32 (2014)
Reitsma, S., Kueper, B.H.: Laboratory measurement of capillary–pressure saturation relationships in a rock fracture. Water Resour. Res. **30**(4), 865–878 (1994)
Rienzner, M., Gandolfi, C.: Investigation of spatial and temporal variability of saturated soil hydraulic conductivity at the field-scale. Soil Tillage Res. **135**, 28–40 (2014)
Rosas, J., Lopez, O., Missimer, T.M., Coulibaly, K.M., Dehwah, A.H.A., Sesler, K., Lujan, L.R., Mantilla, D.: Determination of hydraulic conductivity from grain-size distribution for different depositional environments. Groundwater **52**(3), 399–413 (2014)
Rose, C., Stern, W., Drummond, J.: Determination of hydraulic conductivity as a function of depth and water content for soil in situ. Soil Res. **3**(1), 1–9 (1965)
Rutqvist, J.: Fractured rock stress–permeability relationships from in situ data and effects of temperature and chemical–mechanical couplings. Geofluids **15**(1–2), 48–66 (2015)
Saar, M.O., Manga, M.: Depth dependence of permeability in the Oregon Cascades inferred from hydrogeologic, thermal, seismic, and magmatic modeling constraints. J. Geophys. Res. Solid Earth **109**(B4), 229–245 (2004)
Sakata, Y., Ikeda, R.: Depth dependence and exponential models of permeability in alluvial-fan gravel deposits. Hydrogeol. J. **21**(4), 773–786 (2013)
Welch, L.A., Allen, D.M.: Hydraulic conductivity characteristics in mountains and implications for conceptualizing bedrock groundwater flow. Hydrogeol. J. **22**(5), 1003–1026 (2014)
Youngs, E.G.: Horizontal seepage through unconfined aquifers with hydraulic conductivity varying with depth. J. Hydrol. **3**(3–4), 283–296 (1965)
Youngs, E.G.: Steady state flow around wells in aquifers with hydraulic conductivity varying with depth. Water Resour. Res. **7**(5), 1366–1368 (1971)
Zhang, L., Franklin, J.A.: Prediction of water flow into rock tunnels: an analytical solution assuming an hydraulic conductivity gradient. Int. J. Rock Mech. Min. Sci. Geomech. Abstr. **30**(1), 37–46 (1993)
Zhao, P., Shao, M., Wang, T.: Spatial distributions of soil surface-layer saturated hydraulic conductivity and controlling factors on dam farmlands. Water Resour. Manag. **24**(10), 2247–2266 (2010)